

Demonstration of an Exposed-Core Fiber Platform for Two-Photon Rubidium Spectroscopy

C. Perrella,^{1,*} H. P. Griesser,¹ P. S. Light,¹ R. Kostecki,^{1,2} T. M. Stace,^{3,4} H. Ebendorff-Heidepriem,^{1,2}
T. M. Monro,^{1,5} A. G. White,^{4,6} and A. N. Luiten¹

¹*Institute for Photonics and Advanced Sensing (IPAS) and the School of Physical Sciences,
The University of Adelaide, Adelaide, Australia*

²*ARC Center of Excellence for Nanoscale Biophotonics, Australia*

³*ARC Centre for Engineered Quantum Systems, Australia*

⁴*School of Mathematics and Physics, University of Queensland, Brisbane, Australia*

⁵*The University of South Australia, Adelaide, Australia*

⁶*ARC Centre for Quantum Computing and Communication Technology, Australia*

(Received 9 April 2015; revised manuscript received 18 June 2015; published 22 July 2015)

We demonstrate a promising fiber architecture for generating strong photon-photon interactions. Exposed-core silica optical fibers possess low-loss guidance between 400 and 1700 nm crucial for quantum-logic applications. The potential of this fiber is demonstrated by exciting a two-photon transition within a rubidium vapor using an exposed-core silica optical fiber. Transit-time broadened spectral features enable measurement of the evanescent-field scale length of (120 ± 20) nm which shows excellent agreement with the characteristics of the modeled fiber mode (118 ± 2) nm. We observe a two-photon absorption coefficient of 8.3 cm^{-1} for one optical mode in response to a transmitted power of 1.3 mW in the second mode. A clear pathway to an exposed-core fiber exhibiting substantial absorption mediated by a single photon is identified.

DOI: [10.1103/PhysRevApplied.4.014013](https://doi.org/10.1103/PhysRevApplied.4.014013)

I. INTRODUCTION

Strong photon-photon interactions are a key ingredient to produce the on-demand and deterministic entanglement necessary for a scalable, universal set of quantum-photonics devices [1,2]. The most promising results to date are generated from resonantly enhanced systems [3–5], which recently demonstrated a near-ideal two-photon π phase shift [6]. The resonant nature of these platforms places tight constraints on the interacting photon's frequency and bandwidth. Nonresonant (traveling-wave) systems avoid such restrictions and demonstrate all-optical switching with a few hundred photons [7] and broadband single-photon memories [8,9]. One promising path to creating nonresonant strong photon-photon interactions is the use of two-photon transitions within atomic vapors [10–14]. The efficiency of these higher-order atom-light interactions is directly proportional to optical intensity; thus, an optical arrangement capable of generating high optical intensities at the single-photon level is required.

Two main approaches are used to generate these high-intensity traveling optical fields within atomic vapors. Solid-core optical waveguides [14–20] with core areas of approximately $0.1 \mu\text{m}^2$ produce optical fields outside their core with peak intensities in the range of approximately 6 GW m^{-2} per milliwatt of guided power [21]. Such devices are capable of atom trapping [16,17] and driving two-photon transitions [14]. These nanoscale cores offer large optical

intensities but only short interaction lengths [20], can be fragile, and potentially suffer failure after prolonged operation [19]. A second approach confines a vapor within hollow-core optical waveguides [10–13,22–24]. The minimum core area demonstrated for hollow-core waveguides to date is approximately $16 \mu\text{m}^2$ [25], leading to a maximum peak intensity in the range of approximately 125 MW m^{-2} per milliwatt of guided power, capable of driving two- and three-photon transitions [10–14,23]. Hollow-core waveguides offer long interaction lengths, although this comes at the cost of long vapor-loading times [12,23].

II. EXPOSED-CORE FIBER

Here we present an exposed-core fiber (ECF) architecture that exhibits many of the best features of the aforementioned approaches. Light is guided within the ECF's core, shown in Fig. 1(a), which is suspended from the outer jacket by three struts. An opening through the jacket (which extends along the length of the fiber) allows the surrounding medium access to the optical field that propagates outside the silica core. The peak intensity of the optical field in the surrounding medium is 0.25 MW m^{-2} per milliwatt of guided power for the fiber used here. While currently not demonstrating the same strong evanescent fields of a tapered fiber, the ECF's suspended core architecture offers superior mechanical strength, enabling long fiber lengths to be used which compensate for their lower intensity. In this paper, a 30-cm length of fiber is used, which is 60 times longer than typical tapered-fiber approaches [14]. The exposed-core

*chris.perrella@adelaide.edu.au

architecture alleviates the months required to load hollow-core waveguides [12,23,25], with absorption or fluorescence signatures observed within minutes to hours of exposure to atomic vapor. These attributes make the ECF architecture promising for use in quantum-photonics devices which is demonstrated here via production of photon-photon interactions.

The ECF is manufactured via ultrasonic milling of an F300HQ silica rod to form a preform, which is drawn down into the final fiber diameter on a 6-m fiber tower [26,27]. The resulting ECF has an effective core diameter of $7.5\ \mu\text{m}$ and demonstrates low-loss guidance between 400 and 1700 nm, measured by using a cutback technique over a length of 6.7 m; see Fig. 1(b). The fiber presents a low $(0.12 \pm 0.02)\ \text{dB m}^{-1}$ loss at the wavelengths used in this experiment, which is crucial for single-photon quantum applications. Finite element modeling of the ECF shows the electric field of the fundamental guided mode decays exponentially outside the silica core with a $1/e^2$ intensity scale length of $d = (118 \pm 2)\ \text{nm}$ and $1/e^2$ intensity area of $A = (0.77 \pm 0.05)\ \mu\text{m}^2$ for the wavelengths used here; see Fig. 1(c). Experimental near-field mode images observed from this fiber matched numerical modeling well [see Fig. 1(e)], and power outside the core is due to imaging artifacts. The integrated power in the evanescent field on the exposed side of the core is 7×10^{-5} of the fundamental mode's power.

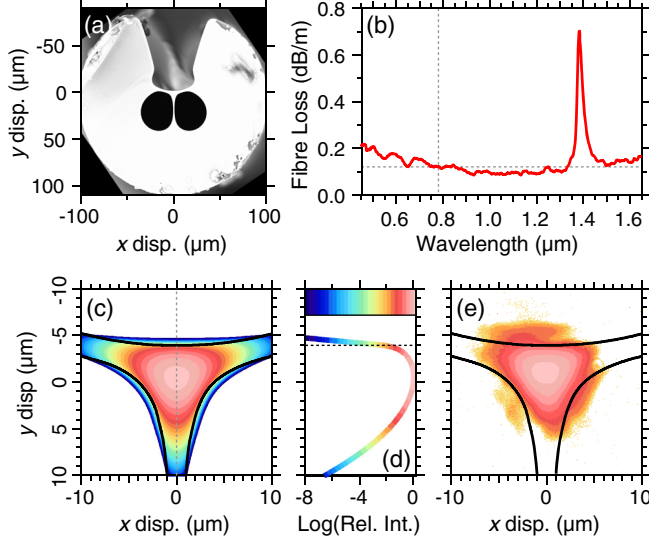


FIG. 1. (a) A scanning electron microscope image of the exposed-core fiber. (b) Cutback loss measurement of ECF showing $< 0.2\ \text{dB m}^{-1}$ loss from 450 to 1650 nm. An OH^- absorption is visible at 1360 nm. Dashed lines indicate the operating wavelength and loss. (c) Finite element model of the power distribution of the fundamental mode. (d) Cross section through the optical mode at $x = 0$, indicated by the dashed line in (c). The horizontal line indicates the edge of the silica core. The scale bar shows color scaling for (c)–(e). (e) Experimental near-field mode image observed from the ECF.

III. EXPERIMENTAL SETUP

To mediate photon-photon interactions, the fiber is surrounded by a rubidium (Rb) vapor which possesses a strong two-photon transition; see Fig. 2(a). The $5S_{1/2} \rightarrow 5D_{5/2}$ two-photon transition of Rb is enhanced via stepwise excitation through the intermediate $5P_{3/2}$ state of linewidth $\Gamma_{5P} = 6.1\ \text{MHz}$. Lasers at 780 and 776 nm, frequencies ω_{780} and ω_{776} , respectively, are tuned to the $5S_{1/2} \rightarrow 5P_{3/2}$ and $5P_{3/2} \rightarrow 5D_{5/2}$ transitions, frequencies ω_{SP} and ω_{PD} , respectively. The $5D_{5/2}$ excited state has a lifetime of 238 ns (linewidth of $\Gamma_{5D} = 666\ \text{kHz}$) with a 7.5% probability of decay via the $6P_{3/2} \rightarrow 5S_{1/2}$ transition to produce 420-nm fluorescence [28]. The 420-nm fluorescence provides a measure of the transition rate into the excited state and thus enables inference of the 780-nm absorption caused by the two-photon transition. Direct observation of the 780-nm absorption is masked by backscattered infrared light from the ECF faces and vacuum windows.

Figure 2(b) shows the optical setup. The 780-nm laser is an extended cavity diode laser, and the 776-nm laser is a titanium:sapphire laser. The 776-nm laser is typically held at a fixed frequency, while the 780-nm is scanned over 10 GHz.

The chamber, containing a $l = 30\ \text{cm}$ length of the ECF, is heated to a temperature of $T = (85 \pm 5)\ ^\circ\text{C}$ to increase the Rb vapor density to $N = (2.2 \pm 0.8) \times 10^{18}\ \text{atoms m}^{-3}$. The two lasers are launched into either end of the ECF to produce counterpropagating fields enabling Doppler-free spectroscopy of the two-photon transition. The beams are coupled through windows at either end of the chamber using 20-mm aspheric lenses. Initially, the transmission through the ECF is $(12.5 \pm 2.5)\%$. The ECF's low loss implies that this is due to poor coupling efficiency from optical-mode mismatch. Exposure to the Rb vapor over a period of 2 months degraded the transmission to $(1.0 \pm 0.2)\%$, associated with a Rb metallic layer on the surface of the fiber's exposed core generating an additional loss of $0.37\ \text{dB cm}^{-1}$. Similar effects are observed with a

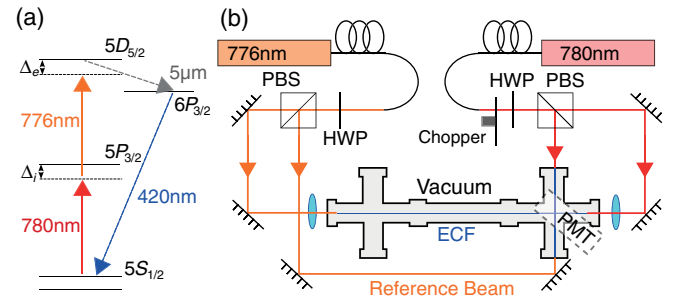


FIG. 2. (a) Energy-level diagram of the two-photon transition used. Excitation lasers (solid lines) and relevant decay paths (dashed) are indicated. (b) Experimental setup: PBS, polarization beam splitter; HWP, half-wave plate; ECF, exposed-core fiber; PMT, photomultiplier tube.

tapered optical fiber [19]. A second pair of laser beams (reference beams) passes through the vacuum chamber to measure the two-photon transition in a free-space vapor.

Two-photon fluorescence from either the ECF or the reference beams is detected by using a photomultiplier tube (PMT) positioned above a vacuum window. A dichroic filter prevents detection of scattered infrared light. During measurements of the fiber, the reference beams are blocked to eliminate background fluorescence. Synchronous detection is used to improve rejection of unwanted backgrounds and increase sensitivity. The 780-nm laser is amplitude modulated with a mechanical beam chopper at 3 kHz which is detected by the PMT as an amplitude modulation imprinted on the two-photon fluorescence. A lock-in amplifier demodulates the PMT output to measure the amplitude of the two-photon fluorescence.

IV. MODELING

The two-photon fluorescence is modeled by using a five-level atomic model, consisting of the intermediate and excited states $|5P\rangle$ and $|5D\rangle$, a decay path $|6P\rangle$, and the two ground states arising from hyperfine splitting, $|5S_1\rangle$ and $|5S_2\rangle$; see Fig. 2(a). In the atomic frame, detuning from the intermediate and two-photon state is expressed as $\Delta_i = \omega_{\text{SP}} - \omega_{780}(1 - v_z/c)$ and $\Delta_e = (\omega_{\text{SP}} + \omega_{\text{PD}}) - \omega_{780}(1 - v_z/c) - \omega_{776}(1 + v_z/c)$, respectively; see Fig. 2(a). States $|5S_1\rangle$ and $|5P\rangle$ are coupled by a laser with Rabi frequency $\Omega_{\text{sp}}(t)$, while a laser of strength $\Omega_{\text{pd}}(t)$ couples the states $|5P\rangle$ and $|5D\rangle$. The $|5P\rangle$, $|5D\rangle$, and $|6P\rangle$ states decay into the ground-state manifold with known branching ratios [28,29]. The evolution of a particular atom crossing an optical mode is governed by the optical Bloch master equations [30]:

$$\begin{aligned} \dot{\rho} = & -i[H, \rho] \\ & + \sum_{5S_i} (\Gamma_{5S_i}^{5P} \mathcal{D}[|5P\rangle\langle 5S_i|] \rho + \Gamma_{5S_i}^{6P} \mathcal{D}[|6P\rangle\langle 5S_i|] \rho) \\ & + \Gamma_{5P}^{5D} \mathcal{D}[|5D\rangle\langle 5P|] \rho + \Gamma_{6P}^{5D} \mathcal{D}[|5D\rangle\langle 6P|] \rho \end{aligned} \quad (1)$$

with interaction Hamiltonian

$$\begin{aligned} H = & \Delta_e |5D\rangle\langle 5D| + \Delta_i |5P\rangle\langle 5P| \\ & + \left(\frac{\Omega_{\text{sp}}(t)}{2} |5P\rangle\langle 5S_1| + \frac{\Omega_{\text{pd}}(t)}{2} |5D\rangle\langle 5P| + \text{H.c.} \right) \\ & + \omega_{6P} |6P\rangle\langle 6P| + \omega_{5S_2} |5S_2\rangle\langle 5S_2|. \end{aligned} \quad (2)$$

The two-photon scattering rate at a given time t is proportional to $S(t) = NAl\Gamma_{5D}\langle 5D|\rho(t)|5D\rangle$, where N is the number density of the Rb vapor, A is the optical-mode area, l is the interaction length, $\Gamma_{5D} = \Gamma_{5P}^{5D} + \Gamma_{6P}^{5D}$ is the excited-state decay rate, and the excited-state population is $\langle 5D|\rho(t)|5D\rangle$.

For conditions where the light-field crossing time is much shorter than the excited-state lifetime, the thermal motion of the atoms cannot be ignored [31,32]. Atoms with different speeds and trajectories will experience different time-dependent Rabi frequencies $\Omega_{\text{sp}}(t)$ and $\Omega_{\text{pd}}(t)$. We average the absorption over the Maxwell-Boltzmann distribution similar to that presented in Ref. [32] by using $\mathcal{F} = F_{v_0}^{(z)}(v_z)F_{v_0}^{(t)}(v_t)$, where $F_{v_0}^{(z)}(v_z)$ is the atoms' axial Maxwell-Boltzmann velocity distribution and $F_{v_0}^{(t)}(v_t)$ is the atoms' transverse Maxwell-Boltzmann speed distribution with $v_0 = (2k_B T/m)^{1/2}$. For a Gaussian beam, the final scattering-rate expression, averaging over axial velocity v_z and transverse speed v_t , takes the form

$$S(\Delta_i, \Delta_e) = \int_{-r}^r \int_0^{2\pi} \int_0^\infty \int_{-\infty}^\infty \mathcal{F} \bar{S}(v_t) dv_t dv_z d\theta dx, \quad (3)$$

where r is the Gaussian mode's electric field $1/e$ half-width. The averaged scattering rate \bar{S} is evaluated by transformation of its parameter space to that of the atomic transit time using the relationship $v_t = d/\tau$, where d is the length of the chord through the Gaussian mode's electric field that the atom passes through, such that $\bar{S}(\tau) = \int_0^\tau S(t) dt$.

In contrast, the elongated aspect ratio of the evanescent field allows us to treat all atoms as if they are leaving the fiber traveling parallel to the y axis of Fig. 1 from $x = 0$. The final scattering rate, averaging over axial velocity v_z and transverse speed v_t , takes the form

$$S(\Delta_i, \Delta_e) = \int_0^\infty \int_{-\infty}^\infty \mathcal{F} \bar{S}(v_t) dv_t dv_z. \quad (4)$$

We calculate the expected line shape from Eqs. (3) and (4) for the two situations, free-space excitation and ECF excitation:

$$S(\Delta_i, \Delta_e) \propto NAlI_{780}I_{776}e^{-(\Delta_i/\sigma_D)^2}L(\Delta_e), \quad (5)$$

where I_{780} and I_{776} are the intensities of the 780- and 776-nm laser, respectively, and $\sigma_D = \omega_{\text{SP}}v_0/c$ is the Doppler broadening of the intermediate state. The line-shape function takes the form

$$L(\Delta_e) = \begin{cases} e^{-n|\Delta_e\bar{\tau}|} & \Gamma_{5D}\bar{\tau} \ll 1, \\ V(\Delta_e, \Gamma_{5P} + \Gamma_{5D}, \sigma_{\text{PT}}) & \Gamma_{5D}\bar{\tau} \gg 1, \end{cases} \quad (6)$$

where the average transit time is $\bar{\tau}$, $V(\Delta_e, \Gamma_{5P} + \Gamma_{5D}, \sigma_{\text{PT}})$ is a Voigt profile with detuning Δ_e , the Lorentzian component full width at half maximum of $\Gamma_{5P} + \Gamma_{5D}$, and $\sigma_{\text{PT}} = v_0(\omega_{\text{PD}} - \omega_{\text{SP}})/c$ is the Doppler broadening Gaussian $1/e$ half-width. For atoms that experience a decaying exponential evanescent-field profile, such as the mode profile of the ECF, $n = 2$, whereas $n = 1$ for a Gaussian optical-mode profile [31].

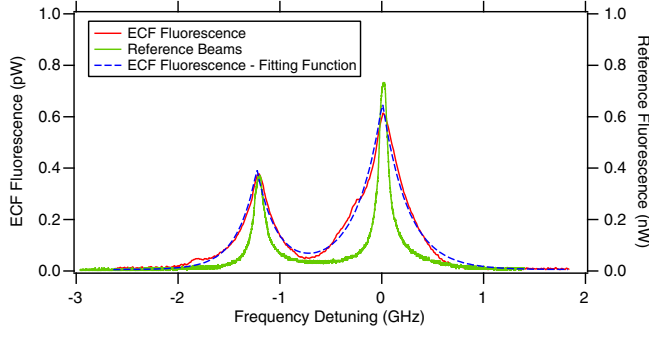


FIG. 3. Fluorescence spectra from the ECF (red line) with fit of the form in Eq. (5) (dashed blue line), the reference beam (green line) as a function of 780-nm detuning from the ^{85}Rb $F_g = 3 \rightarrow F' = 4$ D_2 transition. The ECF spectra show transit-time broadening, whereas the reference is a Voigt profile, both expected from Eq. (6). A frequency shift between the two spectra is subtracted, a result of spectra acquired at different times.

V. RESULTS

A. Spectral line shape

Figure 3 presents experimental measurements of the fluorescence resulting from excitation via free-space reference beams (green line) and with beams guided by the ECF (red line). The spectral line shapes are seen to be consistent with Eqs. (5) and (6): The ECF excitation shows a broadened line shape characteristic of transit-time-limited light-atom interactions, while the free-space excitation shows a more conventional Voigt profile. The free-space vapor fluorescence line shape shows a Voigt profile, with a full width at half maximum of (135 ± 15) MHz produced through strong power broadening of the intermediate $5P_{3/2}$ state, producing an effective broadening of Γ_{5P} [33–35]. Equations (3) and (4) are evaluated in the low-optical-power limit, where $\Omega_{\text{sp}}(t), \Omega_{\text{pd}}(t) < \Gamma_{5D}$ and $\Omega_{\text{sp}}(t), \Omega_{\text{pd}}(t) < \Gamma_{5S_i}^{5P}$. Extending this theory to higher powers produces power broadening on the $|5S_i\rangle \rightarrow |5P\rangle$ transition with a similar dependence reported within Refs. [33–35]:

$$\Gamma_{\text{FWHM}} = \Gamma_{5D} + s\Gamma_{5P}\sqrt{1 + \Omega_{\text{sp}}/\Omega_{\text{sat}}}, \quad (7)$$

where $s = (\omega_{\text{SP}} - \omega_{\text{PD}})/\omega_{\text{SP}}$, for this configuration is $s \approx 0.005$, the intermediate, $|5P\rangle$, state decay rate is $\Gamma_{5P} = \Gamma_{5S_1}^{5P} + \Gamma_{5S_2}^{5P}$, and Ω_{sat} is the transition's effective saturation Rabi frequency. Power broadening of this two-photon transition has previously been experimentally investigated within a hollow-core fiber geometry [12] showing agreement with Eq. (7).

The main feature in Fig. 3 is fluorescence from the Doppler-free two-photon transition excited from the counterpropagating beams. Weaker features are evident when detuning from double resonance ($\Delta_i = 0$, $\Delta_e = 0$), indicated by arrows in Fig. 4. These features originate from the

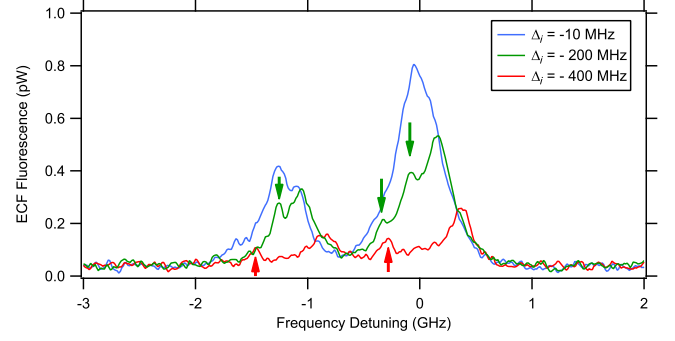


FIG. 4. Fluorescence from the ECF detected at the PMT showing the presence of copropagating fluorescence (indicated by arrows) alongside counterpropagating fluorescence for difference intermediate-state detunings. The frequency axis is relative to the ^{85}Rb D_2 $F_g = 3 \rightarrow F' = 4$ transition.

two-photon transition being excited from copropagating beams originating from backreflections off the fiber end faces. When on resonance with the excited state, the copropagating fluorescence occurs when

$$\Delta_e = \delta_{\text{SP}} + \delta_{\text{PD}} + \frac{v_z}{c}(\omega_{780} + \omega_{776}) = 0, \quad (8)$$

where $\delta_{\text{SP}} = \omega_{\text{SP}} - \omega_{780}$ and $\delta_{\text{PD}} = \omega_{\text{PD}} - \omega_{776}$. The 780-nm laser is on resonance with the velocity class v_z for the intermediate transition $\delta_{\text{SP}} = -\omega_{780}v_z/c$. As a result, Eq. (8) shows that the only atoms that can be excited to the two-photon state are the atoms with a velocity of v_z : $\delta_{\text{PD}} = -\omega_{780}v_z/c$. This tight constraint placed on the atom's velocity due to the copropagating two-photon transition produces narrow velocity-selective spectra.

The co- and counterpropagating contributions tune differently with the driving laser frequencies due to the different laser configurations, seen in Fig. 4. The copropagating fluorescence satisfies Eq. (8), whereas the counterpropagating excitation satisfies the equation

$$\Delta_e = \delta_{\text{SP}} + \delta_{\text{PD}} + \frac{v_z}{c}(\omega_{780} - \omega_{776}) = 0. \quad (9)$$

The result is that the ratio of detunings for the copropagating case follows $\delta_{\text{SP}}/\delta_{\text{PD}} = 1$, whereas the counterpropagating case follows $\delta_{\text{SP}}/\delta_{\text{PD}} = -1$ due to energy conservation.

When doubly resonant, the copropagating and counterpropagating contributions lie at the same frequency, distorting the line shape. This leads to a distortion of the observed transition strength and spectral linewidth which is highlighted in Fig. 5 and discussed below.

B. Transit-time broadening

The Doppler-free counterpropagating two-photon fluorescence signals, shown in Fig. 3, are fitted with Eq. (5), giving an estimate for the average transit time as

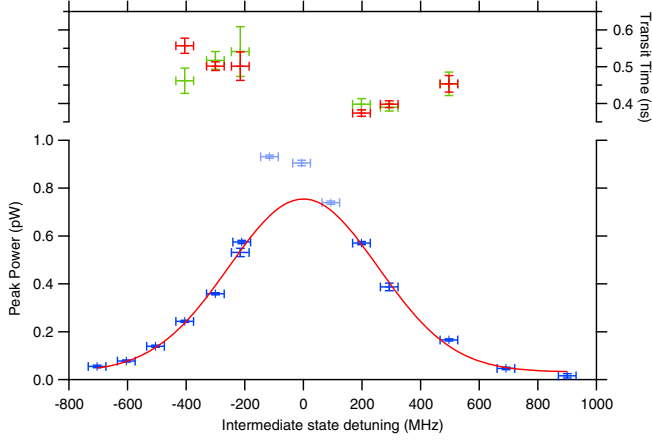


FIG. 5. Transit-time measurements for ^{85}Rb (green) and ^{87}Rb (red) for different intermediate-state detunings Δ_i . Fluorescence amplitude detected at the PMT for the ^{85}Rb $F_g = 3 \rightarrow F'$ transition manifold as a function of intermediate-state detuning Δ_i , for fixed laser intensities I_{780} and I_{776} and $\Delta_e = 0$. Highlighted points are excluded from the Gaussian fit; see the text.

$\bar{\tau} = (470 \pm 80)$ ps. We obtain the same value of $\bar{\tau}$ for both Rb isotopes, and little statistically significant variation is seen as a function of intermediate-state detuning; see Fig. 5. Spectra near resonance with the intermediate transition are not shown, as the results are skewed by the presence of copropagating features overlapping the counterpropagating spectra; see Fig. 4. Combining the measured transit time with the mean thermal velocity $v_0 = (262 \pm 2)$ ms^{-1} at $T = (85 \pm 5)$ $^\circ\text{C}$ predicts an evanescent-field scale length of $d = (120 \pm 20)$ nm, in excellent agreement with the modeled field extent of $d = (118 \pm 2)$ nm.

C. Transition strength

The transition strength is investigated as a function of intermediate-state detuning Δ_i for fixed laser intensities I_{780} and I_{776} and $\Delta_e = 0$; see Fig. 5. It is evident that the transition strength has a predominately Gaussian profile in accord with Eq. (5) associated with inhomogeneous Doppler broadening of the intermediate transition. The three measurements that are doubly resonant ($\Delta_i = 0$, $\Delta_e = 0$), shown lighter in Fig. 5) show additional fluorescence. This effect is due to multiple excitation paths into the excited state that are opened through weak backreflections in the apparatus, seen in Fig. 4. By excluding these points, we find a Gaussian $1/e$ half-width of (360 ± 17) MHz. This behavior is expected from the thermal distribution of Rb atoms in combination with the intermediate-state hyperfine structure, which predicts an intermediate $1/e$ Gaussian half-width of (350 ± 2) MHz.

Figure 6 shows the dependence of the fluorescence on the transmitted powers when driving the ^{85}Rb $F_g = 3$ and ^{87}Rb $F_g = 2$ transitions in double resonance, $\Delta_i = 0$ and $\Delta_e = 0$. The fluorescence shows proportionality to the product of the laser intensities, as expected from Eq. (5).

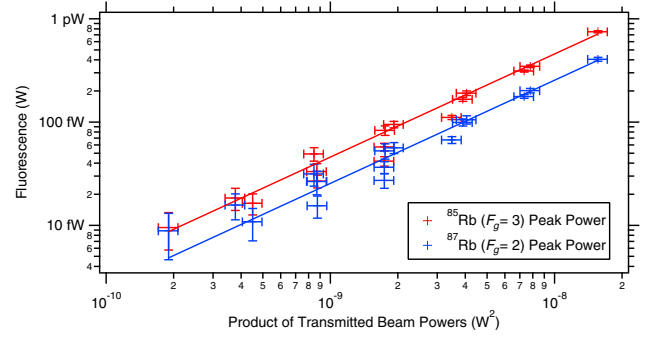


FIG. 6. Fluorescence power detected at the PMT as a function of the product of transmitted laser beam powers.

D. Fiber absorption strength

The key figure of merit for this highly nonlinear platform is the cross sensitivity of the absorption coefficient in one mode to power in the second mode. We need estimates of the fraction of power from each mode that are coupled to the Rb vapor as well as the effective absorption coefficient for the 780-nm beam from the observed fluorescence.

We calculate the absorbed power for the highest powers used in the experiment, which is $12 \mu\text{W}$ and 1.3 mW of transmitted power for the 780- and 776-nm beam, respectively. At these powers, the PMT measures (750 ± 50) fW of 420-nm fluorescence (see Fig. 6), corresponding to 14 nW of fluorescence emitted along the ECF length, accounting for the PMT collection efficiency of 5.4×10^{-5} . The two-photon transition rate is calculated from this by allowing for various decay branches from the excited state: a nonradiative decay branch of 50% due to collision with the silica fiber structure; and only 7.5% of the radiative decays result in 420-nm fluorescence [28]. This yields an absorbed power of $0.2 \mu\text{W}$ corresponding to a fractional absorption of $\mathcal{A} = 1.7\%$ relative to the transmitted 780-nm beam. This corresponds to each atom within the evanescent field scattering an average of 0.4 photons per excited-state lifetime Γ_{5D} .

The absorption coefficient of the two-photon transition, α_{TP} , is related to the fiber's transmission \mathcal{T} , which is expressed in a modified Beer-Lambert law:

$$\mathcal{T} = \mathcal{T}_F / \mathcal{T}_0 (1 - \mathcal{A}) = e^{-l(\alpha_{\text{Rb}} + \alpha_{\text{TP}} F)}, \quad (10)$$

where $\mathcal{T}_F = (1.0 \pm 0.2)\%$ is the transmission of the fiber when detuned from both the two-photon and intermediate transitions, $\mathcal{A} = 1.7\%$ is the two-photon fractional absorption, $\mathcal{T}_0 = (12.5 \pm 2.5)\%$ is the original transmission prior to ECF exposure to Rb, $l = 0.3 \text{ m}$ is the fiber length, $\alpha_{\text{Rb}} = 0.084 \text{ cm}^{-1}$ (corresponding to 0.37 dB cm^{-1}) is the fiber loss due to Rb degradation, and $F = 7 \times 10^{-5}$ is the fraction of the guided mode on the exposed side of the core. Equation (10) suggests that the two-photon absorption coefficient within the evanescent field is

$\alpha_{\text{TP}} = 8.3 \text{ cm}^{-1}$ for the 780-nm beam at the largest powers shown in Fig. 6.

We find that this agrees with that reported in a tapered-fiber experiment [14]. Taking into account a different fraction of power within the evanescent field, interaction length, rubidium vapor temperature, evanescent-field area, and probing power, we find agreement between the two experiments within the knowledge of experimental parameters to show a ratio of $1.0^{+0.9}_{-0.5}$.

VI. DISCUSSION

A clear pathway towards a platform of high utility to the quantum information community can be seen. The next generation of ECF to be manufactured with an effective core size of $1 \mu\text{m}$ would generate intensities outside the silica core of 500 MW m^{-2} per milliwatt of guided power [36,37]. These ECFs would deliver a substantial improvement when compared to the $7.5\text{-}\mu\text{m}$ fiber described here: A $1\text{-}\mu\text{m}$ ECF has a smaller evanescent-field area $A = (0.11 \pm 0.02) \mu\text{m}^2$ and a fraction of the guided mode on the exposed side of the core, $F = 2 \times 10^{-2}$, resulting in approximately 2240 times stronger interaction with the Rb vapor. An additional increase in absorption strength can be gained by elevating the operating temperature to $T = 200 \text{ }^\circ\text{C}$ to increase the Rb density. Under these conditions, a single photon in the 776-nm guided mode per atomic transit time will deliver an absorption coefficient of $\alpha_{\text{TP}} \approx 1 \text{ cm}^{-1}$ in the 780-nm mode resulting in near 50% absorption over the same length fiber. Implementing techniques such as light-induced atomic desorption and fiber heating are shown to eject Rb off fiber surfaces, thus potentially decreasing the fiber loss due to Rb deposition [19,25,38]. Furthermore, separate work shows low-loss splicing of ECF to a conventional solid-core single-mode fiber [39], opening the way to a convenient architecture for generating a strong light atom and, thus, photon-photon interactions via two-photon interactions. A demonstration of this nature would be highly significant for quantum photonics.

VII. CONCLUSION

In conclusion, we demonstrate that ECFs possess low-loss guidance between 400 and 1700 nm, crucial for quantum-logic applications. The potential of this fiber for use in quantum-logic applications is further demonstrated through generating strong photon-photon interactions utilizing the Rb two-photon transition $5S_{1/2} \rightarrow 5D_{5/2}$. A two-photon absorption coefficient of 8.3 cm^{-1} , corresponding to a total absorption of 1.7%, is observed in one laser mode when the second mode is driven with 1.3 mW. Two-photon spectra enable measurement of the evanescent-field scale length to be $(120 \pm 20) \text{ nm}$, in excellent agreement with the modeled fiber mode $(118 \pm 2) \text{ nm}$. Projection to a $1\text{-}\mu\text{m}$ core fiber

shows that a single 776-nm photon per atomic transit time would result in approximately 50% absorption of a 780-nm photon. This architecture offers great promise in the field of all-optical switching or for quantum-logic gates where two-photon absorption at low power levels is required.

ACKNOWLEDGMENTS

The authors acknowledge financial support from the Australian Research Council under Grants No. DP0877938, No. DE120102028, and No. FT0991631. This research is supported by the South Australian Government through the Premier's Science and Research Fund. The authors acknowledge Peter Henry, Stephen Warren-Smith, and Erik Schartner from the University of Adelaide for their contribution to the silica fiber fabrication. This work is performed in part at the OptoFab node of the Australian National Fabrication Facility utilizing Commonwealth and South Australian State Government funding. The authors acknowledge the Australian Defence Science and Technology Organisation (under the Signatures, Materials and Energy Corporate Enabling Research Program) for support of the suspended and exposed-core silica fiber development at The University of Adelaide.

-
- [1] P. Kok, K. Nemoto, T. C. Ralph, J. P. Dowling, and G. J. Milburn, Linear optical quantum computing with photonic qubits, *Rev. Mod. Phys.* **79**, 135 (2007).
 - [2] H. J. Kimble, The quantum internet, *Nature (London)* **453**, 1023 (2008).
 - [3] T. G. Tiecke, J. D. Thompson, N. P. de Leon, L. R. Liu, V. Vuletić, and M. D. Lukin, Nanophotonic quantum phase switch with a single atom, *Nature (London)* **508**, 241 (2014).
 - [4] S. M. Hendrickson, C. N. Weiler, R. M. Camacho, P. T. Rakich, A. I. Young, M. J. Shaw, T. B. Pittman, J. D. Franson, and B. C. Jacobs, All-optical-switching demonstration using two-photon absorption and the Zeno effect, *Phys. Rev. A* **87**, 023808 (2013).
 - [5] J. Goldwin, M. Trupke, J. Kenner, A. Ratnapala, and E. A. Hinds, Fast cavity-enhanced atom detection with low noise and high fidelity, *Nat. Commun.* **2**, 418 (2011).
 - [6] J. Volz, M. Scheucher, C. Junge, and A. Rauschenbeutel, Nonlinear pi phase shift for single fiber-guided photons interacting with a single atom, *Nat. Photonics* **8**, 965 (2014).
 - [7] M. Bajcsy, S. Hofferberth, V. Balic, T. Peyronel, M. Hafezi, A. S. Zibrov, V. Vuletić, and M. D. Lukin, Efficient All-Optical Switching Using Slow Light within a Hollow Fiber, *Phys. Rev. Lett.* **102**, 203902 (2009).
 - [8] M. R. Sprague, D. G. England, A. Abdolvand, J. Nunn, X.-M. Jin, W. Steven Kolthammer, M. Barbieri, B. Rigal, P. S. Michelberger, T. F. M. Champion, P. St. J. Russell, and I. A. Walmsley, Efficient optical pumping and high optical

- depth in a hollow-core photonic-crystal fibre for a broadband quantum memory, *New J. Phys.* **15**, 055013 (2013).
- [9] M. R. Sprague, P. S. Michelberger, T. F. M. Champion, D. G. England, J. Nunn, X.-M. Jin, W. S. Kolthammer, A. Abdolvand, P. St. J. Russell, and I. A. Walmsley, Broadband single-photon-level memory in a hollow-core photonic crystal fibre, *Nat. Photonics* **8**, 287 (2014).
- [10] V. Venkataraman, K. Saha, and A. L. Gaeta, Phase modulation at the few-photon level for weak-nonlinearity-based quantum computing, *Nat. Photonics* **7**, 138 (2013).
- [11] V. Venkataraman, K. Saha, P. Londero, and A. L. Gaeta, Few-Photon All-Optical Modulation in a Photonic Band-Gap Fiber, *Phys. Rev. Lett.* **107**, 193902 (2011).
- [12] C. Perrella, P. S. Light, J. D. Anstie, T. M. Stace, F. Benabid, and A. N. Luiten, High-resolution two-photon spectroscopy of rubidium within confined geometry, *Phys. Rev. A* **87**, 013818 (2013).
- [13] C. Perrella, P. S. Light, J. D. Anstie, F. Benabid, T. M. Stace, A. G. White, and A. N. Luiten, High-efficiency cross-phase modulation in a gas-filled waveguide, *Phys. Rev. A* **88**, 013819 (2013).
- [14] S. M. Hendrickson, M. M. Lai, T. B. Pittman, and J. D. Franson, Observation of Two-Photon Absorption at Low Power Levels Using Tapered Optical Fibers in Rubidium Vapor, *Phys. Rev. Lett.* **105**, 173602 (2010).
- [15] M. Kohonen, M. Succo, P. G. Petrov, R. A. Nyman, M. Trupke, and E. A. Hinds, An integrated atom-photon junction, *Nat. Photonics* **5**, 35 (2011).
- [16] A. Goban, K. S. Choi, D. J. Alton, D. Ding, C. Lacroûte, M. Pototschnig, T. Thiele, N. P. Stern, and H. J. Kimble, Demonstration of a State-Insensitive, Compensated Nanofiber Trap, *Phys. Rev. Lett.* **109**, 033603 (2012).
- [17] E. Vetsch, D. Reitz, G. Sagué, R. Schmidt, S. T. Dawkins, and A. Rauschenbeutel, Optical Interface Created by Laser-Cooled Atoms Trapped in the Evanescent Field Surrounding an Optical Nanofiber, *Phys. Rev. Lett.* **104**, 203603 (2010).
- [18] D. E. Jones, J. D. Franson, and T. B. Pittman, Saturation of atomic transitions using subwavelength diameter tapered optical fibers in rubidium vapor, *J. Opt. Soc. Am. B* **31**, 1997 (2014).
- [19] M. Lai, J. D. Franson, and T. B. Pittman, Transmission degradation and preservation for tapered optical fibers in rubidium vapor, *Appl. Opt.* **52**, 2595 (2013).
- [20] L. Stern, B. Desiatov, I. Goykhman, and U. Levy, Nanoscale light-matter interactions in atomic cladding waveguides, *Nat. Commun.* **4**, 1548 (2013).
- [21] T. M. Monro, W. Belardi, K. Furusawa, J. C. Baggett, N. G. R. Broderick, and D. J. Richardson, Sensing with microstructured optical fibres, *Meas. Sci. Technol.* **12**, 854 (2001).
- [22] W. Yang, D. B. Conkey, B. Wu, D. Yin, A. R. Hawkins, and H. Schmidt, Atomic spectroscopy on a chip, *Nat. Photonics* **1**, 331 (2007).
- [23] G. Epple, K. S. Kleinbach, T. G. Euser, N. Y. Joly, T. Pfau, P. St. J. Russell, and R. Löw, Rydberg atoms in hollow-core photonic crystal fibres, *Nat. Commun.* **5**, 4132 (2014).
- [24] S. Okaba, T. Takano, F. Benabid, T. Bradley, L. Vincetti, Z. Maizelis, V. Yampol'skii, F. Nori, and H. Katori, Lamb-Dicke spectroscopy of atoms in a hollow-core photonic crystal fibre, *Nat. Commun.* **5**, 4096 (2014).
- [25] A. D. Slepko, A. R. Bhagwat, V. Venkataraman, P. Londero, and A. L. Gaeta, Generation of large alkali vapor densities inside bare hollow-core photonic band-gap fibers, *Opt. Express* **16**, 18976 (2008).
- [26] R. Kostecki, H. Ebendorff-Heidepriem, C. Davis, G. McAdam, S. C. Warren-Smith, and T. M. Monro, Silica exposed-core microstructured optical fibers, *Opt. Mater. Express* **2**, 1538 (2012).
- [27] R. Kostecki, H. Ebendorff-Heidepriem, S. Afshar V., G. McAdam, C. Davis, and T. M. Monro, Novel polymer functionalization method for exposed-core optical fiber, *Opt. Mater. Express* **4**, 1515 (2014).
- [28] D. Sheng, A. Pérez Galván, and L. A. Orozco, Lifetime measurements of the 5d states of rubidium, *Phys. Rev. A* **78**, 062506 (2008).
- [29] D. Adam Steck, Rubidium 87 D line data, <http://steck.us/alkalidata> (revision 2.1.4, 23 December 2010).
- [30] D. F. Walls and G. J. Milburn, *Quantum Optics* (Springer-Verlag, Berlin, 2008).
- [31] S. N. Bagayev, V. P. Chebotayev, and E. A. Titov, Saturated absorption lineshape under the transit-time conditions, *Laser Phys.* **4**, 224 (1994).
- [32] T. M. Stace and A. N. Luiten, Theory of spectroscopy in an optically pumped effusive vapor, *Phys. Rev. A* **81**, 033848 (2010).
- [33] J. E. Bjorkholm and P. Liao, Line shape and strength of two-photon absorption in an atomic vapor with a resonant or nearly resonant intermediate state, *Phys. Rev. A* **14**, 751 (1976).
- [34] M. Tanasittikosol, C. Carr, C. S. Adams, and K. J. Weatherill, Subnatural linewidths in two-photon excited-state spectroscopy, *Phys. Rev. A* **85**, 033830 (2012).
- [35] T. T. Grove, V. Sanchez-Villicana, B. C. Duncan, S. Maleki, and P. L. Gould, Two-photon two-color diode laser spectroscopy of the Rb $5D_{5/2}$ state, *Phys. Scr.* **52**, 271 (1995).
- [36] S. C. Warren-Smith, G. Nie, E. P. Schartner, L. A. Salamonsen, and T. M. Monro, Enzyme activity assays within microstructured optical fibers enabled by automated alignment, *Biomed. Opt. Express* **3**, 3304 (2012).
- [37] R. Kostecki, H. Ebendorff-Heidepriem, S. C. Warren-Smith, and T. M. Monro, Predicting the drawing conditions for microstructured optical fiber fabrication, *Opt. Mater. Express* **4**, 29 (2014).
- [38] S. Ghosh, A. R. Bhagwat, C. K. Renshaw, S. Goh, A. L. Gaeta, and B. J. Kirby, Low-Light-Level Optical Interactions with Rubidium Vapor in a Photonic Band-Gap Fiber, *Phys. Rev. Lett.* **97**, 023603 (2006).
- [39] S. C. Warren-Smith, R. Kostecki, L. Viet Nguyen, and T. M. Monro, Fabrication, splicing, Bragg grating writing, and polyelectrolyte functionalization of exposed-core microstructured optical fibers, *Opt. Express* **22**, 29493 (2014).